Analytic bond-order potential for atomistic simulations of zinc oxide

Analytic bond-order potential for atomistic simulations of zinc oxide

Paul Erhart[1]**, Niklas Juslin**[2]**, Oliver Goy**[3]**, Kai Nordlund**[2]**, Ralf Müller**[3]
and Karsten Albe[1]

[1] Institut für Materialwissenschaft, Technische Universität Darmstadt, Petersenstraße 23,
D-64287 Darmstadt, Germany
[2] Accelerator Laboratory, University of Helsinki, PO Box 43, FIN-00014, Finland
[3] Fachbereich Bauingenieurwesen und Geodäsie, Technische Universität Darmstadt,
Hochschulstraße 1, D-64289 Darmstadt, Germany

Abstract
An interatomic potential for zinc oxide and its elemental constituents is derived
based on an analytical bond-order formalism. The model potential provides a
good description of the bulk properties of various solid structures of zinc oxide
including cohesive energies, lattice parameters, and elastic constants. For the
pure elements zinc and oxygen the energetics and structural parameters of a
variety of bulk phases and in the case of oxygen also molecular structures are
reproduced. The dependence of thermal and point defect properties on the cutoff
parameters is discussed. As exemplary applications the irradiation of bulk zinc
oxide and the elastic response of individual nanorods are studied.

1. Introduction

Zinc oxide is a traditional semiconductor with manifold applications in electronic and
optoelectronic devices [1, 2], which more recently has attracted much attention, because
nanostructures such as rods, wires, belts, and rings [3, 4] have been prepared experimentally.

In order to improve the understanding of the physical and chemical properties of zinc
oxide, computer simulations can be a valuable tool, complementing experiments or aiding
their interpretation. Quantum-mechanical methods such as Hartree–Fock (HF) or density-
functional theory (DFT) have been extensively used to investigate, for example, surfaces [5, 6],
high-pressure phase transitions [7–9], elastic properties [9], phonon dispersion [10], and point
defects (see, e.g., [11–16]) in ZnO. While such methods are highly transferable and allow
for accurate and reliable calculations, they are computationally very demanding. Atomistic
simulations of multi-million atom systems that go beyond nanoseconds in time are therefore
only possible if the electronic degrees of freedom are removed and interatomic potentials
are introduced, which are computationally more efficient. Upon reducing the complexity of
the system some information is inevitably lost, but a sensibly chosen potential scheme in

combination with a carefully constructed fitting database can nevertheless realistically mimic the chemical bonding and structure of solids.

Metal oxides represent an especially difficult case for atomistic modelling because of their complex electronic structure and intricate mixture of ionicity and covalency. Therefore, very few potentials have been devised and most of them are shell-model potentials that are not capable of describing the elemental components (see section 2). The situation is further complicated if the system of interest features such diverse phases as a hexagonal close-packed metal (zinc), a gaseous phase (dimeric oxygen), and a ionic–covalent semiconductor (zinc oxide). In the following, we briefly review potential schemes which have been previously used to model compounds with ionic and ionic–covalent bonding characteristics. In doing so we motivate our interest in exploring the applicability of a purely covalent model to zinc oxide, which can be considered a prototype for other oxide systems. In section 4 a concise summary of the potential formalism adopted in the present work is given. Sections 5, 6, and 7 introduce and discuss the potentials for Zn–O, Zn–Zn, and O–O interactions, respectively. Finally, the potential is applied in simulations of the irradiation of bulk zinc oxide and to study the elastic response of individual nanorods (section 9).

2. Review of potential schemes

The bonding and structure of many elemental metals and semiconductors can be reasonably described by analytic potentials that have been used in a wide range of applications [17–23]. With regard to compounds, the situation is more complex, as in most systems cohesion arises from a mixture of covalent, ionic and van der Waals interactions. Formally, the cohesive energy can be written as a sum of these contributions, and if a realistic description of the bonding behaviour is pursued, one needs to assess the relative weight and the mathematical representations of each of these terms. In the following, potential schemes from the literature are compared, focusing on the treatment of covalency versus ionicity, and, where applicable, charge equilibration.

The alkaline halides and alkaline earth oxides are typical examples of ionic compounds in which long-range Coulomb interactions between the ions dominate. Simple Born–Mayer potentials which combine a Coulomb potential with a short-ranged, spherically symmetric repulsive potential are usually sufficient in order to obtain a satisfactory description. Shell-model potentials (see, e.g., [24–26]) represent a somewhat more refined approach combining short-ranged repulsive, long-ranged dispersive, and ionic interactions with a simple, usually harmonic, model for atomic polarizability [27]. The ionic charges are kept fixed at their nominal values (and independent of the atomic environment). In the past, shell-model potentials have been applied to a wide range of materials since they offer a very handy formalism with few fitting parameters and yield useful models when only a small section of configuration space is of relevance. Since three-body interactions are not explicitly taken into account, covalent contributions either have to be neglected or are subsumed in the fitting parameters. The formalism is incapable of describing pure elements, which renders it inapt for simulations which include the boundary phases of the material. Furthermore, due to the long range of the Coulomb potential the treatment of electrostatic interactions is computationally very demanding. In dynamical simulations the shells must be assigned a fictitious mass which is usually much smaller than the mass of the atoms in the system. A very small time step must, therefore, be chosen which further increases the computational load compared to other potential schemes.

In contrast to ionic interactions, covalent bonding is characterized by strong directional bonds, and therefore angle-dependent many-body terms need to be taken into account. By

merging Stillinger–Weber type [28] two- and three-body potentials with terms describing Coulomb, monopole–dipole, and van der Waals interactions, Vashishta and co-workers arrived at a scheme capable of describing materials such as silicon carbide [29, 30], gallium arsenide [31], and zinc oxide [32]. The ions are assigned fixed, effective charges and the long-range electrostatic interactions are truncated at some intermediate distance, reducing the computational effort substantially. The potentials are designed such that the boundary phases can be described on the same basis as the compound.

In an effort to simulate metal/metal oxide systems, Streitz and Mintmire devised a scheme (ES+) which merges the embedded-atom method (EAM) with an ionic potential [33]. The model explicitly accounts for charge transfer between anions and cations by equilibrating the ionic charge for each configuration which renders it computationally very demanding. The scheme has been applied with some success for modelling alumina [33] and with modifications to titania [34].

More recently, Duin *et al* constructed a reactive force field (ReaxFF) which features a combination of many-body, van der Waals, and Coulomb terms [35]. Originally designed for hydrocarbons, the scheme is also sufficiently flexible to describe oxidic compounds and metals, as shown for the case of alumina [36]. Similar to the Vashishta potentials, the Coulomb potential is truncated at some distance, while the effective ionic charges are determined via charge equilibration in a similar way to the Streitz–Mintmire approach. The full functional form features 93 parameters. Many degrees of freedom for fitting increase the flexibility of the potential scheme but parameter space sampling becomes tremendously complex and the risk of generating spurious minima in the potential hypersurface grows.

Purely covalent bonding exemplified by elemental semiconductors such as carbon, silicon, or germanium can be well described within the bond-order approach pioneered by Abell [37] and Tersoff [38] and later extended by Brenner [39]. It turns out the formalism works similarly well for strongly covalent compounds. The bond-order formalism was shown to be formally equivalent to the embedded-atom method (EAM) which has been very successful in modelling metallic bonding [40]. In fact, it turns out that the bond-order ansatz is capable of describing many pure metals (including transition metals) on the same footing as covalent materials [21, 23]. Therefore, it is possible to derive a consistent set of potentials which describe the compound as well as its components within a single formalism.

Pettifor and co-workers were able to show that bond-order potentials can be rigorously derived within tight-binding theory based on a moment expansion of the density of states [41, 42]. They later extended their approach to higher moments and multi-component systems [43]. The scheme has been applied to obtain potentials for example for hydrocarbons [44], but oxide materials have not been considered so far.

3. Motivation

In this work, we pursue the question whether it is possible to treat a highly ionic compound such as zinc oxide within a purely covalent model. The neglect of charges avoids the computationally expensive treatment of long-range interactions, and therefore allows one to obtain an atomistic model which is significantly more efficient than any of the formally ionic potentials described in the foregoing section.

We employ an analytic bond-order potential (ABOP) scheme [21, 20] which has already been successfully applied to a number of systems including purely metallic [21, 23], predominantly covalent [45, 20, 18], molecular [22] as well as mixed ionic–covalent bonding [23, 22]. Thus, the ABOP scheme in principle offers the possibility to describe the Zn–O, O–O as well as Zn–Zn interactions within a single framework. Although it turns out

that for many situations the neglect of charges is legitimate, it needs to be acknowledged that the applicability of the ABOP is limited if internal or external electric fields become dominant, as in the case of interfaces or surfaces. The restriction to first-nearest neighbours also implies that the energy difference between the zinc blende and the wurtzite structures becomes zero, since their local environments are indistinguishable. The ABOP, however, performs very well in reproducing a variety of bulk properties including cohesive energies, structures, and elastic properties, as will be shown in the next sections.

We anticipate the analytic bond-order potential presented in this work to be useful for atomistic simulations of a variety of phenomena and processes as exemplified in section 9.

4. Methodology

The bond-order potential scheme and the fitting strategy used in this work have been extensively described elsewhere (see, e.g., [20, 21]). Differences in the fitting strategy are pointed out where applicable. For completeness, in the following, we briefly summarize the functions needed to calculate the potential energy. For fitting the parameter sets we employed the recently developed PONTIFIX code which provides a simple fitting interface for deriving parameter sets for the ABOP scheme [46].

In the ABOP scheme, the total energy is written as a sum over individual bond energies

$$E = \sum_{i>j} f_{ij}^c(r_{ij}) \left[V_{ij}^R(r_{ij}) - \underbrace{\frac{b_{ij} + b_{ji}}{2}}_{\overline{b_{ij}}} V_{ij}^A(r_{ij}) \right] \tag{1}$$

where for the pair-like attractive and repulsive terms Morse-like pair potentials are adopted:

$$V^R(r) = \frac{D_0}{S-1} \exp\left(-\beta\sqrt{2S}(r-r_0)\right),$$
$$V^A(r) = \frac{SD_0}{S-1} \exp\left(-\beta\sqrt{2/S}(r-r_0)\right). \tag{2}$$

The parameters in these equations are the dimer bond energy D_0, the dimer bond distance r_0 and the parameter S which determines the slope of the Pauling plot (see [21] and figures 1 and 5). The parameter β can be obtained from the ground-state oscillation frequency of the dimer. The cutoff function restricts the range of the interaction to first or second nearest neighbours

$$f^c(r) = \begin{cases} 1 & r \leqslant R_c - D_c \\ \frac{1}{2} - \frac{1}{2}\sin\left[\frac{\pi}{2}(r-R_c)/D_c\right] & |r - R_c| \leqslant D_c, \\ 0 & r \geqslant R_c + D_c \end{cases} \tag{3}$$

where D_c and R_c are adjustable parameters. Explicit three-body interactions are included via the bond-order parameter

$$b_{ij} = (1 + \chi_{ij})^{-\frac{1}{2}}, \tag{4}$$

$$\chi_{ij} = \sum_{k(\neq i,j)} f_{ik}^c(r_{ik}) g_{ik}(\theta_{ijk}) \exp[2\mu_{ik}(r_{ij} - r_{ik})]. \tag{5}$$

The indices monitor the type-dependence of the parameters, which is of importance for the description of compounds. The angular dependence is described by

$$g(\theta) = \gamma \left(1 + \frac{c^2}{d^2} - \frac{c^2}{d^2 + (h + \cos\theta)^2}\right). \tag{6}$$
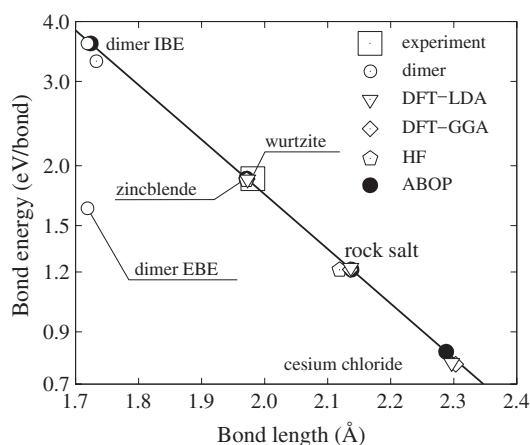
Figure 1. Pauling plot for zinc oxide comparing the analytic bond-order potential (ABOP) with data from experiment, Hartree–Fock (HF) and density-functional theory (DFT) calculations.

Table 1. Parameter sets for describing Zn–Zn, O–O, and Zn–O interactions. R_c^e, D_c^e: cutoff parameters derived for the pure elements; R_c, D_c: default cutoff parameters for simulations of ZnO (see section 8).

Parameter	Zn–Zn	O–O	Zn–O
D_0 (eV)	0.6470	5.166	3.60
r_0 (Å)	2.4388	1.2075	1.7240
S	1.8154	1.3864	1.0455
β (Å^{-1})	1.7116	2.3090	1.8174
γ	4.3909×10^{-5}	0.82595	0.019335
c	77.916	0.035608	0.014108
d	0.91344	0.046496	0.084028
$h\ [\theta_c]$	1.0	0.45056	0.30545
	[180°]	[116.8°]	[107.8°]
2μ (Å^{-1})	0.0	0.0	0.0
R_c^e (Å)	3.00	2.10, 2.60	—
D_c^e (Å)	0.20	0.20	—
R_c (Å)	2.85	2.45	2.60
D_c (Å)	0.20	0.20	0.20

The parameter sets for Zn–Zn, O–O, and Zn–O derived in this work are given in table 1 and will be discussed in the following sections. Cutoff parameters derived for the pure elements are denoted R_c^e and D_c^e, while the parameters appropriate for simulations of the compound ZnO are given in rows R_c and D_c.

5. Zinc oxide

Our fitting methodology requires data on cohesive energies, lattice constants, and elastic constants of a variety of structures in order to cover a range of coordinations as wide as possible. For zinc oxide a plethora of data from experiment and quantum-mechanical calculations is available which could be used for fitting and benchmarking the potential. Therefore, no additional reference calculations were necessary. In order to simplify fitting we transformed the experimentally measured hexagonal elastic constants to the cubic system by means of Martin's transformation method [47] and included the latter values in the fitting database.

Table 2. Summary of properties of the ZnO dimer. Experimental data from [48], data from quantum-mechanical calculations from [49, 50]; EBE: extrinsic bond energy (eV); IBE: intrinsic bond energy (eV); r_0: bond length (Å); ω_0: ground state oscillation frequency (cm^{-1}); IBE, r_0 and ω_0 are given for the dissociation of the dimer ground state into higher energy atomic states (T1: $ZnO(X\ ^1\Sigma) \rightarrow Zn(^1S) + O(^1D)$).

	Expt.	Theory	ABOP
EBE	1.61 ± 0.04	1.20–1.63	
IBE	3.58	3.31, 3.60	3.60
r_0		1.679–1.771	1.724
ω_0	805 ± 40	646–913	708

5.1. Dimer properties

As the pair parameters of the ABOP are usually adjusted to dimer data, we begin by discussing the properties of the ZnO molecule. The dimer behaves peculiarly in the way that its ground state dissociates into excited atomic states (T1: $ZnO(X\ ^1\Sigma^+) \rightarrow Zn(^1S) + O(^1D)$) while the dissociation into the atomic ground states occurs from an excited state of the dimer (T2: $ZnO(a\ ^3\Pi) \rightarrow Zn(^1S) + O(^3P)$). This implies that the lowest experimentally determined dimer energy (associated with the extrinsic bond energy, EBE) cannot be described by a single pair potential but corresponds to a crossing over of the potentials describing the transitions T1 and T2, respectively [48, 50]. For consistency, we only consider the dimer energy, bond length and oscillation frequency which describe transition T1, that is the decomposition of the dimer ground state into the excited atomic states (intrinsic bond energy, IBE). The parameter set given in table 1 yields very good agreement with both the experimental and the quantum-mechanically computed data for this transition, as shown in table 2.

5.2. Bulk properties

The performance of the ABOP with respect to bulk properties is compared to experiment and DFT calculations in table 3. The energy difference between the wurtzite and zinc blende structures is zero due to the neglect of long-range interactions. For the same reason the axial ratio ($c/a = \sqrt{8/3}$) as well as the internal relaxation parameter ($u = 3/8$) of the wurtzite structure are restricted to their ideal values. Otherwise, the agreement with respect to cohesive energies, volumes and bulk moduli is excellent. In particular, the elastic constants of the wurtzite phase compare very well with experiment. In table 3 we also give the elastic constants of wurtzite calculated directly with the values obtained by Martin's transformation method from the elastic constants of the zinc blende structure, and find very good agreement.

The semi-logarithmic plot of bond energies versus bond lengths in figure 1 reveals an almost perfect agreement with the Pauling relation. By applying the common-tangent construction to the energy–volume curves shown in figure 2 one obtains the transition pressure for the wurtzite–rock salt transformation as 10 GPa, in good agreement with experimental values in the range of 8.6–10 GPa as well as first-principles calculations predicting transition pressures between 8.6 and 14.5 GPa (see [56] and references therein).

The comparison also includes the shell-model potential by Lewis and Catlow (LC) [24, 25], which is computationally much more expensive than the ABOP. For our calculations with the LC potential we employed the General Utility Lattice Program (GULP) [60]. The LC potential yields elastic constants in good agreement with experiment but reveals some deficiencies in the description of the equilibrium volumes and energies of the rock salt and zinc blende phases.

Table 3. Summary of bulk properties of zinc oxide as obtained from the analytic bond-order potential (ABOP) in comparison with data from experiment [51–55], density-functional theory (DFT) [9, 56, 7, 8, 57, 58] and Hartree–Fock (HF) [7, 57] calculations as well as the shell-model potential due to Lewis and Catlow (LC) [24, 25]. E_c: cohesive energy (eV/f.u.); ΔE: energy difference with respect to ground-state structure (eV/f.u.); V_0: equilibrium volume (Å^3/f.u.); a: lattice constant (Å); c/a: axial ratio; u: internal parameter of wurtzite structure; B, B': bulk modulus (GPa) and its pressure derivative. c_{ij}: elastic constants (GPa); c_{44}^0: unrelaxed shear modulus of zinc blende structure (GPa); ζ: Kleinman parameter [59].

| | Experiment | ABOP | Quantum-mechanical calculations | | | |
			LDA-DFT	GGA-DFT	HF	LC
			Zinc blende ($F\bar{4}3m$), no. 216, B3			
ΔE		0.0[a]	0.015	0.013	0.052	0.097
a		4.552	4.509	4.633	4.614	4.547
B	145[b]	144	162	135	157	144
B'		4.4	4.0	3.7	3.6	3.6
c_{11}	193[b]	192				175
c_{12}	121[b]	122				129
c'^c	36[c]	36				23
c_{44}	54[b]	56				106
c_{44}^0		149				
ζ		0.72				
			Wurtzite ($P6_3mc$), no. 186, B4			
E_c	−7.52	−7.52	−9.769	−7.692	−5.658	−39.92[d]
V_0	23.61	23.59	22.874	24.834	24.570	23.46
a	3.242[c]	3.219	3.199	3.292	3.290	3.268
c/a	1.6003[c]	1.6330	1.6138, 1.604	1.6076	1.593	1.553
u	0.3819[c]	0.3750	0.3790	0.3802, 0.381	0.3856	0.3920
B	136–183	14 (144[b])	162, 138, 160	134, 125	154	143
B'	3.6–4	4.4	4.1, 4.4	3.8	3.6	3.3
c_{11}	207, 210	212 (210[b])	209	230		236
c_{12}	121	116 (117[b])	85	82		112
c_{13}	106, 105	109 (108[b])	95	64		105
c_{33}	210, 211	219 (220[b])	270	247		188
c_{44}	43, 45	43 (41[b])	46	75		74
c_{66}^c	45, 44	48 (47[b])	62	74		62
			Rock salt ($Fm\bar{3}m$), no. 225, B1			
ΔE		0.237	0.158	0.237	0.242	0.095
a	4.271–4.283	4.275	4.229	4.345	4.225, 4.294	4.267
B	170–228	200	206, 205	173	203, 132	192
B'	3.5–4	4.7	3.9, 4.9	3.7	3.6, 3.8	3.7
			Caesium chloride ($Pm\bar{3}m$), no. 221, B2			
ΔE		0.976	1.307	1.358		1.555
a		2.642	2.624	2.705		2.605
B		218	194	157		216
B'		5.0	4.0	3.8		3.8

[a] Due to restriction to first neighbours.
[b] Transformed from the hexagonal/cubic elastic constants using Martin's transformation method [47].
[c] Cubic: $c' = (c_{11} − c_{12})/2$; hexagonal: $c_{66} = (c_{11} − c_{12})/2$.
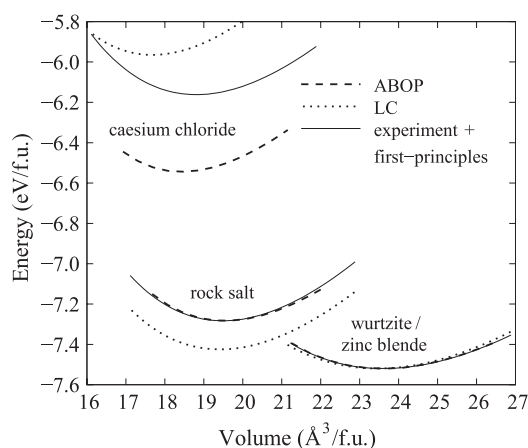[d] This value includes the atomic ionization energy.

Figure 2. Energy–volume curves for bulk structures of zinc oxide illustrating the good agreement between the analytic bond-order potential (ABOP) and the reference curves which were obtained by combining data from experiment and first-principles calculations. The transition pressure can be obtained from this plot by means of the common tangent construction which is equivalent to finding the crossing point of the enthalpy curves. For the Lewis–Catlow shell-model potential (LC) the cohesive energy of the wurtzite structure was set to the experimental value (see footnote in table 3).
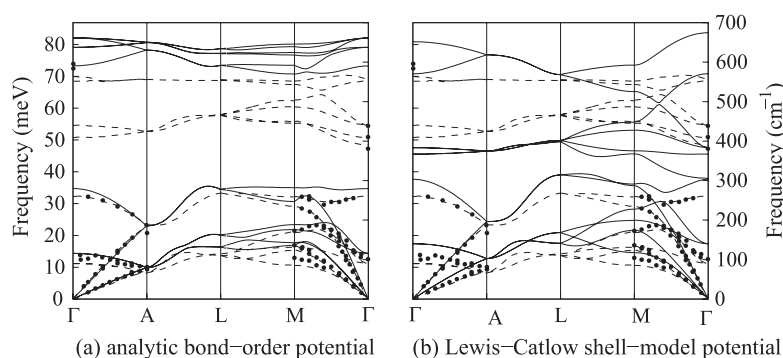

Figure 3. Phonon dispersion relations for (a) the analytic bond-order potential (——) developed in the present work and (b) the shell-model potential by Lewis and Catlow. Dashed lines (- - - -) and black circles (●) show data from density-functional theory calculations and experiment, respectively [10].

As a final test, we have evaluated the phonon dispersion for wurtzite with the ABOP and the LC potential and compared the results with experiment and quantum-mechanical calculations as shown in figure 3 ([10] and references therein). The ABOP shows a very good agreement with the experimental and first-principles data for the lower six branches of the dispersion relation. The deviations are somewhat larger for the LC potential but the overall agreement is still reasonable. On the other hand, the differences are more significant for the upper six (optical) branches. The LC potential yields qualitatively the correct shapes of these bands but fails to predict the phononic band gap and largely overestimates the splittings. In contrast, the ABOP underestimates the splitting of the bands but successfully predicts the existence of a phononic band gap. The shortcomings of both potentials in the description of the higher-lying branches are related to an overestimation (LC) or respectively an underestimation (ABOP) of

the ionicity of the bond and the atomic polarizabilities. In particular the very good description of the lower branches is very encouraging with respect to the applicability of the ABOP.

6. Zinc

Since Zn–Zn interactions are practically absent in the compound, they have to be fitted independently of the Zn–O parameter set. Although the role of d-electrons is *per se* not taken into account in the ABOP scheme (compare section 2), it has turned out that the transition metals platinum [21] and tungsten [23] can be very well described within the ABOP framework. While this experience is encouraging with respect to fitting a similar potential for zinc, it must be acknowledged that the 3d-electrons in zinc have a much more pronounced effect on the bonding behaviour than in platinum or tungsten, most prominently embodied by the unusually large axial ratio of hcp-Zn. Keeping these considerations in mind, we are aiming to obtain a parametrization that can be used in conjunction with the Zn–O parameter set but is not primarily intended to be employed for simulations of pure zinc. It should also be recalled that in the past attempts to model zinc using the embedded-atom method (EAM) and modified EAM schemes have essentially failed [65, 66].

Within the ABOP scheme it turns out to be impossible to reproduce all properties equally well with a single parameter set. In particular, due to the short-ranged nature of the potential it is very difficult to reproduce the fcc–hcp energy difference (and thus the stacking fault energy) realistically. We have therefore focused on obtaining a reasonable fit to the energies and equilibrium volumes of various structures and accepted larger deviations in the elastic constants and the hcp axial ratio. (The potential gives $c_{33} > c_{11}$ and $c_{13} < c_{12}$ in contrast to the experiment since the abnormally large axial ratio, which is connected to these inequalities, cannot be reproduced.)

The fitting database comprised data from experiment and calculations. As information on low-coordinated structures is not available in the literature, we performed additional density-functional theory (DFT) calculations on several hypothetical bulk phases as described in the appendix.

6.1. Dimer properties

The Zn_2 molecule is a van der Waals dimer with a very low binding energy on one hand and a very large bond length on the other hand. Since dispersion interactions are not taken into account in the ABOP scheme (compare equations (1), and (2)), we made no attempt to fit the dimer properties but instead treated D_0 and r_0 as adjustable parameters. It is noteworthy that the final values of $D_0 = 0.647$ eV and $r_0 = 2.439$ Å are comparable in magnitude to the Morse parameters describing the second excited state [67] $(4p)^1\Sigma_u^+$ (the first excited state is also of the van der Waals type). For this state *ab initio* calculations yield bond energies between 1.00 and 1.13 eV (bond lengths between 2.65 and 2.97 Å), while values of 1.12 and 1.30 eV have been derived from experiment (bond length 3.30 Å, [67] and references therein).

6.2. Bulk properties

Table 4 provides an overview of the performance of the ABOP with respect to bulk properties in comparison with experiment and DFT calculations. The potential reproduces the energetics very well; the largest deviation from the DFT calculations occurs for the low-coordinated diamond structure. The lattice parameters and bulk moduli are also in good overall agreement with the reference data, as illustrated in figure 4.
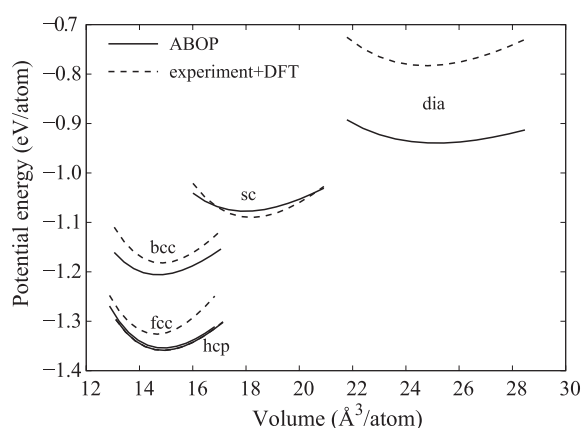
Figure 4. Energy–volume curves for bulk structures of zinc as obtained from the analytic bond-order potential (ABOP) in comparison with reference curves which were obtained by combining data from experiment and density-functional theory (DFT) calculations.

The vacancy formation enthalpy and volume have been determined as 0.4 eV and $-0.3\,\Omega_0$ (Ω_0: atomic volume) which is in reasonable agreement with the experimental values of 0.5 eV and $-0.6\,\Omega_0$ [68]. For the interstitial a formation enthalpy of 2.7 eV and a formation volume of $1.7\,\Omega_0$ have been calculated. Experimentally, a formation volume of $3.5\,\Omega_0$ has been determined but the formation enthalpy is unknown [68].

6.3. Melting behaviour

The melting behaviour of elemental zinc has been investigated by means of molecular dynamics simulations of a solid–liquid interface [69]. The simulation cell contained 768 atoms. The system was equilibrated at zero pressure at temperatures between 0 and 1000 K for at least 0.5 ns. Temperature and pressure were controlled using the Berendsen temperature and pressure controls [70] with coupling constants of 100 and 200 fs, respectively. For temperatures below 650 K and above 685 K either complete solidification or complete melting was observed, while for intermediate temperatures the interface was stable for at least 2 ns. This observation agrees very well with the experimental melting point of 693 K.

7. Oxygen

In order to reproduce the O_2 molecule a simple pair potential would be sufficient, but then the thermodynamically most stable phase would be a close-packed structure (either hexagonal or cubic). In the present work we aim to obtain a more general representation of the bonding behaviour of oxygen.

The fitting database comprised experimental data on the dimer and ozone molecules complemented by data from first-principles calculations (see the appendix). The bond energy, bond length and oscillation frequency of the dimer fix the parameters D_0, r_0 and β. The bond angle of the ozone molecule determines h. Thus there are four parameter left to be fitted. The parameter set which gave the best overall agreement with the input data is given in table 1. The properties calculated with the ABOP are compared in table 5 to experiment and quantum-mechanical calculations. Data sets are given for two different choices of the cutoff parameter R_c^e. The first value ($R_c^e = 2.10$ Å) reproduces the experimental data for the bond angle as well as the cohesive energy of the ozone molecule but the cohesive energies of the higher-

Table 4. Compilation of bulk properties of zinc as calculated using the analytic bond-order potential (ABOP) in comparison with experiment [61, 62, 53, 63] and density-functional theory (DFT, literature data from [64]) calculations. Symbols as in table 3 but energies and volumes are given in units per atom.

| | | DFT | | |
	Experiment	Literature	This work	ABOP
Hexagonal close-packed ($P6_3/mmc$, no. 194, A3)
E_c	-1.359			-1.359
V_0	14.90^a	14.53	14.90	14.88
a	2.660^a	2.607	2.581	2.764
c	4.863^a	4.937	4.791	4.498
c/a	1.8282^a	1.8937	1.8563	1.627
B	73	78	(100^b)	73
B'	4.8		5.4	5.6
c_{11}	165			136
c_{12}	31			47
c_{13}	50			35
c_{33}	62			146
c_{44}	40			37
$c_{66}{}^c$	67			51
Face-centred cubic ($Fm\bar{3}m$, no. 225, A1)
ΔE		0.033	0.032	0.005
a		3.85	3.90	3.91
B		95	95	72
B'		4.2	5.1	5.6
Body-centred cubic ($Im\bar{3}m$, no. 229, A2)
ΔE		0.177	0.106	0.149
a		3.07	3.11	3.07
B		84	89	67
B'		5.1	5.2	5.5
Diamond ($Fd\bar{3}m$, no. 227, A4)
ΔE			0.576	0.419
a			5.72	5.86
B			40	25
B'			5.1	5.2
Simple cubic ($Pm\bar{3}m$, no. 221, A_h)
ΔE			0.270	0.281
a			2.54	2.62
B			65	43
B'			5.1	5.4

[a] At 0 K as cited in [64].
[b] Energy–volume curve obtained at fixed axial ratio, $c/a = 1.8563$.
[c] $c_{66} = (c_{11} - c_{12})/2$.

coordinated structures are systematically overestimated. The longer cutoff ($R_c^e = 2.60$ Å) yields a superior description of the higher-coordinated phases but sacrifices the ozone molecule. The good overall agreement of the oxygen–oxygen parameter set with the reference data is further illustrated by the Pauling plot shown for $R_c^e = 2.60$ Å in figure 5.
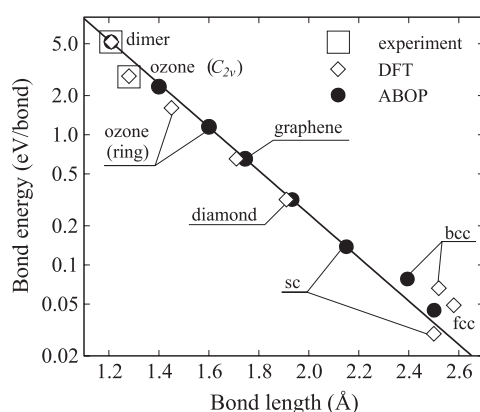
Figure 5. Pauling plot for oxygen. The solid line illustrates the Pauling relation while the symbols correspond to data from experiment, density-functional theory (DFT) and the analytic bond-order potential (ABOP) calculations. The deviation of the ABOP data points from the Pauling plot for larger bond lengths is due to the penetration of the cutoff range ($R_c^e = 2.60$ Å).

8. Defect properties, melting, and the role of cutoff parameters

The geometries and the energetics of point defects in zinc oxide result from an intricate interplay of electronic effects leading to rather complicated configurations such as the oxygen dumbbell interstitials [76–78]. The existence of many different stable charge states furthermore leads to a strong dependence of the formation enthalpies on the Fermi level. Obviously, these complications are impossible to capture in any analytic potential scheme, which owes its efficiency to the neglect of the electronic structure. For modelling of an ensemble of several hundred or thousand atoms, it is, however, usually sufficient to have a reasonable description of the energetics, while defect geometries play a minor role. Therefore, no attempt has been made to reproduce the defect structures obtained from quantum mechanical calculations with the analytic bond-order potential.

The bond-order potential scheme used in the present work employs a cutoff function in order to scale the interaction to zero between the first and second nearest neighbour shells. Therefore, the cutoff parameters can be varied within a certain range without affecting the ground state properties considered during fitting (cohesive energies, lattice parameters, elastic constants). On the other hand, the cutoff parameters do affect other properties such as point defect formation enthalpies, melting behaviour, or migration barriers. In the past the cutoff parameters of existing potentials have been occasionally modified in order to optimize them for certain applications, e.g., in the context of point defect properties [79, 45] or in the study of large volumetric deformations [80].

The ABOP developed in the foregoing sections was therefore tested with respect to variations of the cutoff parameters. The impact on point defect formation enthalpies can be rationalized as follows.

- The vacancy formation enthalpies are unaffected by the cutoff distances. The extent of relaxation around the vacant site is obviously insufficient for any of the participating atoms to enter the cutoff region and/or for atoms of the same type to interact.

- The introduction of surplus zinc atoms leads to direct Zn–Zn interactions whence the formation enthalpies of zinc interstitials and antisites are strongly dependent on the zinc cutoff distance. The dependence is typically monotonic but discontinuous. On the other

Table 5. Cohesive energies and structural parameters of oxygen molecules and bulk phases calculated with the analytic bond-order potential (ABOP) in comparison with experimental data [61] and quantum-mechanical (QM) calculations [71–75]. E_c: cohesive energy (eV/atom), ΔE: energy difference with respect to oxygen dimer (eV/atom); r_b: bond length (Å); θ: bond angle of ozone molecule (deg); a: lattice constant (Å).

| | | QM calculations | | ABOP | |
	Experiment	Literature	This work	$R_c^e = 2.1$ Å	2.6 Å
		Dimer			
r_b	1.21	1.22–1.25	1.21	1.21	
E_c	−2.58	−2.24 to −3.07	−2.85	2.58	
		Ozone, ground-state, C_{2v}			
r_b	1.28	1.27–1.39	1.28	1.35	1.40
θ	116.8	116.0		116.8	178.7
ΔE	0.49	0.48–0.67	0.47	0.50	0.83
		Ozone, equilateral triangle (ring)			
r_b		1.45	1.45	1.60	
ΔE		0.90–1.13	0.98	1.43	
		O_4 molecule			
r_b			1.80	1.81	
ΔE			2.26	1.81	
		Graphene sheet			
r_b			1.71	1.75	
ΔE			1.60	1.60	
		Diamond ($Fd\bar{3}m$, no. 227, A4)			
a			4.40	4.46	
ΔE			1.95	1.95	
		Simple cubic ($Pm\bar{3}m$, no. 221, A_h)			
a			2.50	2.07	2.15
ΔE			2.49	2.08	2.17
		Body-centred cubic ($Im\bar{3}m$, no. 229, A2)			
a			2.91	2.43	2.76
ΔE			2.32	2.12	2.27
		Face-centred cubic ($Fm\bar{3}m$, no. 225, A1)			
a			3.65	3.03	3.54
ΔE			2.29	2.14	2.31

hand their dependence on the oxygen cutoff distance is comparably small but usually continuous. The formation enthalpies of oxygen interstitials and antisites which involve oxygen surplus display the inverse behaviour of their zinc-surplus counterparts.

• The formation enthalpies for oxygen-surplus defects are virtually independent of the Zn–O cutoff distance. On the other hand, the zinc-surplus defects display some variation which, however, cannot be easily rationalized, as the dependence on R_c^{Zn-O} itself is sensitive to the choice of R_c^{Zn-Zn} and R_c^{O-O}.

These observations show that the formation enthalpies of zinc and oxygen-surplus point defects (in high-symmetry positions) to some extent can be controlled independently. Vacancies are, however, exempt from this possibility as their formation enthalpies are independent of the cutoff distances. Note that since the ABOP is an atomistic model, it cannot capture the Fermi level dependence of the formation enthalpies of charged defects (see, e.g., [11–14]).

Zinc oxide does not melt congruently but dissociates into liquid zinc and gaseous oxygen. Therefore, the melting point cannot be obtained from simulations of a liquid–solid interface (as done for example in section 6.3 and [69]). Simulations of single-crystalline ZnO cells, however, show qualitatively an increase of thermal stability with increasing Zn–O cutoff distance.

In table 1 a set of cutoff parameters (R_c, D_c) is given that is suitable for simulations of compound systems, which has been tested in a variety of simulations and which has also been used for the applications presented below. Before the present potential is used in any simulation, it is nonetheless advisable to consider the effect of the cutoff parameters explicitly with respect to the application in mind.

9. Applications

9.1. Irradiation of bulk zinc oxide

The threshold displacement energy measures which kinetic energy given to a lattice atom in a certain direction is required in order to produce at least one stable lattice defect [81, 82]. It is a fundamental quantity in irradiation physics, and the first step towards understanding the extent and kind of damage produced by any kind of energetic particle irradiation of a lattice [83]. The definition of this quantity is, however, not unique since the probability to produce a defect does not always rise steeply from zero to one at a certain energy [82]. For a more profound understanding one needs to analyse the integrated displacement probability function [84], i.e. the probability to form a defect at a given energy. In order to determine this function for zinc oxide, molecular dynamics simulations were carried out employing the analytic bond-order potential derived in this work (see also [85]).

First, a cell with 2280 atoms was equilibrated at 5 K and zero pressure. Then a randomly chosen atom near the centre of the cell was assigned a recoil energy in a randomly chosen lattice directions. The evolution of the system was followed for 6 ps. For each recoil atom and direction the energy was successively raised starting from 4 eV in steps of 4 eV until a defect was found. About 1000 O and Zn (atom type and direction) combinations were simulated. Since some threshold experiments were carried out with electron irradiation on single-crystal samples in the *c*-axis direction, another set of simulations was carried out with recoils directed along the positive ('Zn face') *c*-axis direction, assuming an electron beam angular spread of 15° about the [0001] direction. Due to the 4 eV step size all threshold values reported below have an uncertainty of ±2 eV.

Voronoy polyhedron defect analysis centred on the perfect atom sites was used to determine whether a defect had formed at the end of the simulation [86]. Both Voronoy interstitials and vacancies as well as antisites were counted as defects. In addition, if the final energy of the cell was at least 3.7 eV (the minimum energy to form a Frenkel pair) higher than the initial one, a defect was assumed to have formed as well.

Figure 6 shows the integrated displacement probability function [84], i.e. the probability to form a defect at a given energy considering all (atom and direction) combinations simulated. The figure shows that although the minimum threshold energy is about the same for both Zn and O recoils, the defect production efficiency increases much more slowly for O recoils. The defect production probabilities for Zn recoils along arbitrary directions and for recoils along the *c*-axis are similar.
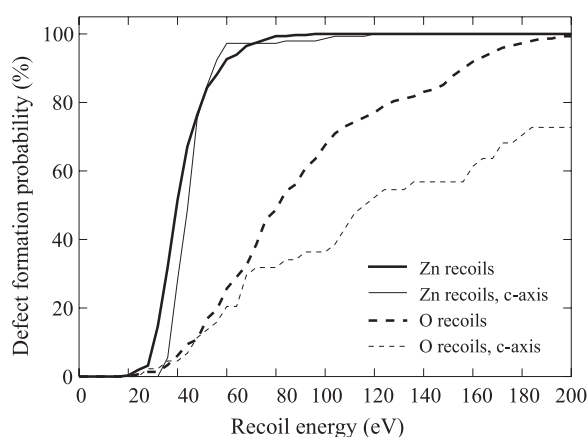
Figure 6. Probability to form a defect during a recoil event in ZnO as a function of energy. Note that the data illustrate specifically the probability to form *at least* one defect; of course at higher energies in many cases more than one defect is formed.

Threshold values for Zn recoils of 57 eV at 313 K [87] and 56 eV at 5 K [88] have been determined from electron irradiation experiments. These studies were carried out on ZnO single crystals in the *c*-axis direction. More recently, using ion irradiation, an effective upper limit threshold for Zn recoils of 65 eV was determined [89]. In electron irradiation experiments the high-energy data are fitted to a linear function and the threshold energy is obtained as the intersection with the energy axis. Since at energies clearly above the threshold, the overall damage production is determined by the average threshold displacement energy, the electron irradiation threshold is most appropriately compared to the average threshold energy. Note that in [88] the actual defect production data are clearly higher than the linear fit to the lowest data points, which can be regarded as an indication for a small defect production probability even below the average threshold, consistent with the observations in the simulations. The present simulations give an average threshold energy of 42 eV for all directions, and 45 eV along the *c*-axis direction. These values are thus in reasonable agreement with the experimental values of <65 eV [89] and 56–57 eV [87, 88], respectively.

For oxygen recoils the experimental data are more difficult to interpret. Optical absorption methods have not detected any defects which can be attributed to the O threshold [88]. (The threshold energy interpretations reported in [90] were later disputed [87].) Electron paramagnetic resonance and electrical measurements have detected an onset of damage at 310 keV electron energy, corresponding to an O recoil energy of 55 eV [87]. It should be noted, however, that the maximum electron irradiation energy in this experiment was only about 680 keV, corresponding to an O recoil energy of 155 eV. This signal may thus be related to the low fractional defect production probabilities observed in the simulations for oxygen recoils in the energy range 20–155 eV.

9.2. Elastic properties of nanorods

In recent years a variety of zinc oxide nanostructures such as rings, belts, rods, wires, and pillars with intriguing properties have been fabricated (see, e.g., [3, 91–93]). They are currently intensively investigated because of potential applications in nanoscale photonics and sensing devices. For many applications the elastic properties of these structures are crucial; on the nanometre scale they are strongly size dependent. Experimentally, the mechanical properties

of individual nanorods or nanotubes can be probed by means of atomic force microscopy as demonstrated for example for silicon carbide nanorods, carbon nanotubes [94], and molybdenum sulfide nanotube ropes [95]. To the best of our knowledge, the elastic response of individual zinc oxide nanorods has, however, not been experimentally characterized. Previous theoretical studies have investigated the response of zinc oxide nanowires under tensile loading [96]. In the present work, we are interested in the behaviour of individual nanorods under shear load resembling the situation in an atomic force microscopy experiment [94, 95]. To this end, we employed conjugate gradient minimization and analysed the results in terms of linear elastic beam theory.

Prismatic zinc oxide nanorods oriented along [0001] were created with diameters ranging from 3 to 12 nm and heights between 8 and 156 nm. The nanorods were placed on [0001]-oriented ZnO substrates with fixed bottom layers. This mimics the effect of a stiff bulk layer underneath. In order to test the impact of the elastic deformation substrate all simulations were also carried out with all substrate atoms fixed. Periodic boundary conditions were imposed in the (0001) plane. First, the atoms in the nanorod were displaced to impose a specified shear strain. Then, the entire system was relaxed using conjugate gradient minimization with the atoms in the top layer tethered in the $[2\bar{1}\bar{1}0]$ direction. This procedure was repeated for different shear strains.

The elastic energy stored in a beam subject to a force F which causes a displacement u is

$$E_{\text{st}} = \tfrac{1}{2}Fu.$$

Taking into account both shearing and bending of the beam, and assuming constant stiffnesses EI and $GA\kappa$, one obtains [97]

$$E_{\text{st}} = \frac{1}{2}\left(\underbrace{\frac{h^3}{3EI}}_{\text{bending}} + \underbrace{\frac{h}{GA\kappa}}_{\text{shearing}} \right)^{-1} u^2$$

where E and G are Young's modulus and the shear modulus, I is the moment of inertia of the beam, and d and h are the diameter and the height of the beam, respectively, A is the cross section, and κ is a geometry factor which takes into account the shape of the cross section. Replacing the displacement by the shear strain $\gamma = u/h$ and dividing by the volume $V = Ah$ yields

$$E_{\text{st}}/V = \tfrac{1}{2}c^*\gamma^2$$

with the effective elastic modulus

$$c^* = \left(\frac{1}{G\kappa} + \frac{Ah^2}{3EI} \right)^{-1}.$$

For a hexagonal cross section, the moment of inertia is $I = 5\sqrt{3}d^4/512$, the geometry factor is $\kappa = 0.901$, and the cross section is $A = 3\sqrt{3}d^2/8$. Introducing the aspect ratio $\beta = h/d$, the effective modulus is given by

$$c^* = \left(\frac{1}{G\kappa} + \frac{64\beta^2}{5E} \right)^{-1}. \tag{7}$$

For the present geometry the ABOP yields $E = 178$ GPa and $G = c_{44} = 43$ GPa.

As shown in figure 7 the elastic response of nanorods is strongly size dependent. Open symbols indicate the results obtained for a completely rigid substrate while filled symbols correspond to simulations in which only the bottom layer was fixed. Since in the latter case the substrate can be deformed, the effective shear moduli are systematically lower than in the case of a fully rigid substrate.
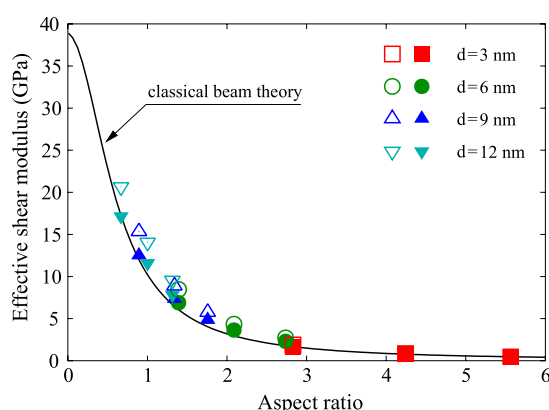
Figure 7. Dependence of the effective shear modulus on the aspect ratio of the nanorods. Open symbols indicate simulations in which all substrate atoms were fixed, while filled symbols correspond to simulations in which only the bottom layer of the substrate was fixed.

(This figure is in colour only in the electronic version)

The solution obtained from classical beam theory given by equation (7) is indicated by the solid line in figure 7. On the present length scales one would assume that surface relaxations and nonlinear contributions, which are captured by the ABOP, lead to a pronounced deviation from a continuum description. The agreement between the atomistic simulations and the continuum model is, however, very good even for very small dimensions. Since equation (7) works reliably for the very small nanorods investigated in the present work, it is reasonable to assume that it is also applicable for much larger nanorods.

10. Conclusions

We have derived an analytic bond-order potential for zinc oxide which describes ZnO as a predominantly covalently bonded system. Since the interatomic potential developed in this work is short-ranged it is computationally more efficient than ionic potentials which require the evaluation of long-ranged Coulombic interactions. The neglect of charges has some drawbacks in the sense that explicit electrostatic effects which play a role for example at surfaces due to unscreened charges cannot be captured. Otherwise the ABOP provides a very good description of many properties of zinc oxide.

The Zn–O parameterization is complemented by parameter sets for the elemental phases of zinc and oxygen. The zinc potential yields a good description of the coordination dependence of the bond lengths and cohesive energies although the elastic constant are not entirely satisfactorily described. The oxygen potential is capable of describing oxygen molecules as well as several hypothetical bulk phases. Thereby, the present potential is applicable in simulations which require a thermodynamic model for the entire Zn–O system. In particular, it is suitable for simulations of ZnO under oxygen-rich or zinc-rich conditions.

The applicability of the potential has been demonstrated through two examples, namely the determination of threshold displacement energies in ZnO and the study of the elastic response of individual nanorods.

Acknowledgments

Appendix. Total energy calculations

In order to apply the fitting strategy outlined previously [21, 20], the energy differences and bond lengths of various bulk structures with different coordinations have to be included in the fitting database. For zinc oxide a broad data basis is available but for zinc and oxygen, further input was required.

A.1. Zinc

Singh and Papaconstantopoulos [64] calculated cohesive energies and lattice parameters of the face-centred cubic (fcc), body-centred cubic (bcc) and hexagonal close-packed (hcp) structures based on density-functional theory (DFT) calculations using the linearized-augmented plane-waves (LAPW) method. We complemented these data with plane-wave pseudo-potential (PWPP) calculations on the lower-coordinated simple cubic (sc) and diamond (dia) structures. These calculations were carried out within the local-density approximation (LDA) in the Teter–Pade parameterization [98] using the PWPP code ABINIT [99][4]. We employed the norm-conserving pseudo potentials due to Troullier and Martins (TM) [100] including the 3d-electrons as part of the valence. We used a plane-wave cutoff-energy of 70 Ha. Brillouin zone sampling was performed employing 572 (hcp), 570 (fcc), 240 (bcc), 570 (dia) and 220 (sc) k-points distributed on shifted Monkhorst–Pack meshes. With these parameters a convergence better than 1 meV/atom was achieved. The calculated energy–volume curves shown in figure 4 were fitted to the Birch–Murnaghan equation of state [101]. The results are summarized in table 4. The agreement with experimental data and previous theoretical work is very good. The systematic underestimation of the lattice constants as compared to experiment is a well-known deficiency of the LDA.

A.2. Oxygen

A wealth of experimental as well as theoretical data is available for the O_2 and O_3 molecules (see, e.g., [61, 71–75]). Additional calculations were performed on higher-coordinated molecules and bulk structures. The CASTEP code [102, 103] was used to perform DFT calculations within the spin-polarized generalized gradient approximation (GGSA) based on the Perdew–Wang parameterization [104] (PW91), and the Gaussian94 code [105] for DFT calculations using the BLYP [106] and B3LYP [107] functionals as well as for Hartree–Fock calculations. Preliminary tests proved the GGSA-PW91 DFT method to be reliable, so it was selected for the further computations.

For the calculations, ultrasoft pseudopotentials were used, employing a plane wave cutoff energy of 380 eV (norm-conserving pseudopotentials were also considered and gave basically identical results); finite basis set corrections were included to compensate for imperfect Brillouin zone sampling. The number of k-points was chosen to obtain convergence of the total energy better than 15 meV/atom. Using these parameters the relaxed structures and cohesive energies of several molecules and bulk structures were computed. In the case of the O_3 molecule the ground state as well as the equilateral triangle geometry, which is known to be a local minimum on the potential energy surface (see, e.g., [75]), were considered. For

---

[4] The ABINIT code is a common project of the Université Catholique de Louvain, Corning Incorporated, and other contributors (URL http://www.abinit.org).

the O_4 molecule the tetrahedron geometry was considered. The higher-coordinated structures comprised graphene as well as diamond, sc, bcc, and fcc. The data are shown in table 5. Where comparison is possible the DFT data computed in the present work are in very good agreement with experiment and previous quantum mechanical calculations.

References

[1] Look D C, Claflin B, Alivov Y I and Park S J 2004 *Phys. Status Solidi* a **201** 2203
[2] Özgür U, Alivov Y I, Liu C, Teke A, Reshchikov M, Doğan S, Avrutin V, Cho S J and Morkoç H 2005 *J. Appl. Phys.* **98** 041301
[3] Pan Z W, Dai Z R and Wang Z L 2001 *Science* **291** 1947
[4] Huang M H, Mao S, Feick H, Yan H, Wu Y, Kind H, Weber E, Russo R and Yang P 2001 *Science* **292** 1897
[5] Jaffe J E, Harrison N M and Hess A C 1994 *Phys. Rev.* B **49** 11153
[6] Kresse G, Dulub O and Diebold U 2003 *Phys. Rev.* B **68** 245409
[7] Jaffe J E and Hess A C 1993 *Phys. Rev.* B **48** 7903
[8] Jaffe J E, Snyder J A, Lin Z and Hess A C 2000 *Phys. Rev.* B **62** 1660
[9] Ahuja R, Fast L, Eriksson O, Wills J M and Johansson B 1998 *J. Appl. Phys.* **83** 8065
[10] Serrano J, Romero A H, Manjón F J, Lauck R, Cardona M and Rubio A 2004 *Phys. Rev.* B **69** 094306
[11] Kohan A F, Ceder G, Morgan D and Van de Walle C G 2000 *Phys. Rev.* B **61** 15019
[12] Zhang S B, Wei S H and Zunger A 2001 *Phys. Rev.* B **63** 075205
[13] Oba F, Nishitani S R, Isotani S, Adachi H and Tanaka I 2001 *J. Appl. Phys.* **90** 824
[14] Erhart P, Albe K and Klein A 2006 *Phys. Rev.* B **73** 205203
[15] Erhart P and Albe K 2006 *Phys. Rev.* B **73** 115207
[16] Erhart P and Albe K 2006 *Appl. Phys. Lett.* **88** 201918
[17] Daw M S, Foiles S M and Baskes M I 1993 *Mater. Sci. Rep.* **9** 251
[18] Albe K and Möller W 1998 *Comput. Mater. Sci.* **10** 111
[19] Brenner D W 2000 *Phys. Status Solidi* b **217** 23
[20] Albe K, Nordlund K, Nord J and Kuronen A 2002 *Phys. Rev.* B **66** 035205
[21] Albe K A, Nordlund K and Averback R S 2002 *Phys. Rev.* B **65** 195124
[22] Nord J, Albe K, Erhart P and Nordlund K 2003 *J. Phys.: Condens. Matter* **15** 5649
[23] Juslin N, Erhart P, Träskelin P, Nord J, Henriksson K, Salonen E, Nordlund K and Albe K 2005 *J. Appl. Phys.* **98** 123520
[24] Catlow C R A 1977 *Proc. R. Soc.* A **353** 533
[25] Lewis G V and Catlow C R A 1985 *J. Phys. C: Solid State Phys.* **18** 1149
[26] Binks D J and Grimes R W 1993 *J. Am. Ceram. Soc.* **76** 2370
[27] Dick B G Jr and Overhauser A W 1958 *Phys. Rev.* **112** 90
[28] Stillinger F H and Weber T A 1985 *Phys. Rev.* B **31** 5262
[29] Shimojo F, Ebbsjö I, Kalia R K, Nakano A, Rino J P and Vashishta P 2000 *Phys. Rev. Lett.* **84** 3338
[30] Chatterjee A, Kalia R, Nakano A, Omeltchenko A, Tsuruta K, Vashishta P, Loong C K, Winterer M and Klein S 2000 *Appl. Phys. Lett.* **77** 1132
[31] Rino J P, Chatterjee A, Ebbsjö I, Kalia R K, Nakano A, Ebbsjö F and Vashishta P 2002 *Phys. Rev.* B **65** 195206
[32] Kubo M, Oumi Y, Takaba H, Chatterjee A, Miyamoto A, Kawasaki M, Yoshimoto M and Koinuma H 2000 *Phys. Rev.* B **61** 16187
[33] Streitz F H and Mintmire J W 1994 *Phys. Rev.* B **50** 11996
[34] Ogata S, Iyetomi H, Tsuruta K, Shimojo F, Kalia R K, Nakano A and Vashishta P 1999 *J. Appl. Phys.* **86** 3036
[35] van Duin A C T, Dasgupta S, Lorant F and Goddard W A III 2001 *J. Phys. Chem.* A **105** 9396
[36] Zhang Q, Çagin T, van Duin A, Goddard W A III, Qi Y and Hector L G Jr 2004 *Phys. Rev.* B **69** 045423
[37] Abell G C 1985 *Phys. Rev.* B **31** 6184
[38] Tersoff J 1988 *Phys. Rev.* B **37** 6991
[39] Brenner D W 1990 *Phys. Rev.* B **42** 9458
[40] Brenner D W 1989 *Phys. Rev. Lett.* **63** 1022
[41] Horsfield A P, Bratkovsky A M, Fearn M, Pettifor D G and Aoki M 1996 *Phys. Rev.* B **53** 12694
[42] Pettifor D and Oleinik I 1999 *Phys. Rev.* B **59** 8487
[43] Pettifor D G, Finnis M W, Nguyen-Manh D, Murdick D A, Zhou X W and Wadley H N G 2004 *Mater. Sci. Eng.* A **365** 2
[44] Oleinik I and Pettifor D 1999 *Phys. Rev.* B **59** 8500
[45] Erhart P and Albe K 2005 *Phys. Rev.* B **71** 035211

[46] Erhart P and Albe K *Pontifix/Pinguin: A Program Package for Fitting Interatomic Potentials of the Bond-Order Type* http://www.mm.mw.tu-darmstadt.de/pontifix

[47] Martin R M 1972 *Phys. Rev.* B **6** 4546
     Martin R M 1979 *Phys. Rev.* B **20** 818 (erratum)

[48] Fancher C A, de Clercq H L, Thomas O C, Robinson D W and Bowen K H 1998 *J. Chem. Phys.* **109** 8426

[49] Boldyrev A I and Simons J 1997 *Mol. Phys.* **92** 365

[50] Bauschlicher C W Jr and Partridge H 1998 *J. Chem. Phys.* **109** 8430

[51] Albertsson J, Abrahams S C and Kvick A 1989 *Acta Crystallogr.* B **45** 34

[52] Kisi E H and Elcombe M M 1989 *Acta Crystallogr.* C **45** 1867

[53] Every A and McCurdy A 1992 *Numerical Data and Functional Relationships in Science and Technology* (*Landolt-Börnstein New Series* vol III/29A) (Heidelberg: Springer)

[54] Bateman T B 1962 *J. Appl. Phys.* **33** 3309

[55] Kobiakov I B 1980 *Solid State Commun.* **35** 305

[56] Desgreniers S 1998 *Phys. Rev.* B **58** 14102

[57] Recio J M, Pandey R and Luaña V 1993 *Phys. Rev.* B **47** 3401

[58] Karzel H, Potzel W, Köfferlein M, Schiessl W, Steiner M, Hiller U, Kalvius G M, Mitchell D W, Das T P, Blaha P, Schwarz K and Pasternak M P 1996 *Phys. Rev.* B **53** 11425

[59] Kleinman L 1962 *Phys. Rev.* **128** 2614

[60] Gale J D and Rohl A L 2003 *Mol. Simul.* **29** 291

[61] Lide D R (ed) 2004 *Handbook of Chemistry and Physics* 85th edn (Boca Raton, FL: CRC Press)

[62] Eisenmann B and Schäfer H 1988 *Numerical Data and Functional Relationships in Science and Technology* (*Landolt-Börnstein New Series* vol III/14 A) (Heidelberg: Springer)

[63] Ledbetter H M 1977 *J. Phys. Chem. Ref. Data* **6** 1181

[64] Singh D and Papaconstantopoulos D A 1990 *Phys. Rev.* B **41** 8885

[65] Cleri F and Rosato V 1993 *Phys. Rev.* B **48** 22

[66] Baskes M I and Johnson R A 1994 *Modelling Simul. Mater. Sci. Eng.* **2** 147

[67] Czajkowski M A, Bobkowski R and Krause L 1990 *Phys. Rev.* A **41** 277

[68] Ehrhart P, Jung P, Schultz H and Ullmaier H 1991 *Numerical Data and Functional Relationships in Science and Technology* (*Landolt-Börnstein New Series* vol III/25) (Heidelberg: Springer)

[69] Ercolessi F, Tomagnini O, Iarlori S and Tosatti E 1993 *Nanosources and Manipulation of Atoms Under High Fields and Temperatures: Applications* ed V T Binh (Dordrecht: Kluwer) pp 185–205

[70] Berendsen H J C, Postma J P M, Gunsteren W F, Nola A D and Haak J R 1984 *J. Chem. Phys.* **81** 3684

[71] Hay P J and Dunning T H Jr 1977 *J. Chem. Phys.* **67** 2290

[72] Curtiss L A, Raghavachari K, Trucks G W and Pople J A 1991 *J. Chem. Phys.* **94** 7221

[73] Seminario J M 1994 *Int. J. Quantum Chem.* **52** (Suppl. 28) 655

[74] Politzer P and Lane P 2000 *Int. J. Quantum Chem.* **77** 336

[75] Jalbout A F 2002 *J. Mol. Struct.: Theochem* **617** 5

[76] Lee E C, Kim Y S, Jin Y G and Chang K J 2001 *Phys. Rev.* B **64** 085120

[77] Janotti A and Van de Walle C G 2006 *J. Cryst. Growth* **287** 58

[78] Erhart P, Klein A and Albe K 2005 *Phys. Rev.* B **72** 085213

[79] Jäger H U and Albe K 2000 *J. Appl. Phys.* **88** 1129

[80] Tang M and Yip S 1995 *Phys. Rev.* B **52** 15150

[81] Averback R S and Diaz de la Rubia T 1998 *Solid State Phys.* **51** 281

[82] Nordlund K, Wallenius J and Malerba L 2006 Molecular dynamics simulations of threshold displacement energies in Fe *Nucl. Instrum. Methods* B **246** 322

[83] Smith R (ed) 1997 *Atomic & Ion Collisions in Solids and at Surfaces: Theory, Simulation and Applications* (Cambridge: Cambridge University Press)

[84] Erginsoy C, Vineyard G H and Englert A 1964 *Phys. Rev.* **133** 595

[85] Look D C, Farlow G C, Reunchan P, Limpijumnong S, Zhang S B and Nordlund K 2005 *Phys. Rev. Lett.* **95** 225502

[86] Nordlund K, Ghaly M, Averback R S, Caturla M, Diaz de la Rubia T and Tarus J 1998 *Phys. Rev.* B **57** 7556

[87] Meese J M and Locker D R 1972 *Solid State Commun.* **11** 1547

[88] Pazionis G and Schulz H J 1986 *Mater. Sci. Forum* **10–12** 839

[89] Lorenz K, Alves E, Wendler E, Bilani O, Wesch W and Hayes M 2005 *Appl. Phys. Lett.* **87** 191904

[90] Vehse W E, Sibley W A, Keller F J and Chen Y 1968 *Phys. Rev.* **167** 828

[91] Park W I, Kim D H, Jung S W and Yi G C 2002 *Appl. Phys. Lett.* **80** 4232

[92] Law M, Goldberger J and Yang P 2004 *Annu. Rev. Mater. Sci.* **34** 83

[93] Fan H J, Lee W, Hauschild R, Alexe M, Le Rhun G, Scholz R, Dadgar A, Nielsch K, Kalt H, Krost A, Zacharias M and Gosele U 2006 *Small* **2** 561
[94] Wong E W, Sheehan P E and Lieber C M 1997 *Science* **277** 1971
[95] Kis A, Mihailovic D, Remskar M, Mrzel A, Jesih A, Piwonski I, Kulik A J, Benoît W and Forró L 2003 *Adv. Mater.* **15** 733
[96] Kulkarni A J, Zhou M and Ke F J 2005 *Nanotechnology* **16** 2749
[97] Schnell W, Gross D and Hauger W 1992 *Technische Mechanik 2–Elastostatik* (Berlin: Springer)
[98] Goedecker S, Teter M and Hutter J 1996 *Phys. Rev.* B **54** 1703
[99] Gonze X, Beuken J M, Caracas R, Detraux F, Fuchs M, Rignanese G M, Sindic L, Verstraete M, Zerah G, Jollet F, Torrent M, Roy A, Mikami M, Ghosez P, Raty J Y and Allan D 2002 *Comput. Mater. Sci.* **25** 478
[100] Troullier N and Martins J L 1991 *Phys. Rev.* B **43** 1993
[101] Birch F 1978 *J. Geophys. Res.* **83** 1257
[102] Accelrys Inc 2001 *CASTEP Users Guide* (San Diego, CA: Accelrys Inc)
[103] Milman V, White J A, Pickard C J, Payne M C, Akhmatskaya E V and Nobes R H 2000 *Int. J. Quantum Chem.* **77** 895
[104] Perdew J P 1991 *Electronic Structure of Solids* ed P Ziesche and H Eschrig (Berlin: Akademie)
[105] Frisch M J and Trucks G W 1995 *Gaussian 94, rev. E.2* (Pittsburgh, PA: Gaussian)
[106] Lee C, Yang W and Parr R G 1988 *Phys. Rev.* B **37** 785
[107] Becke A D 1993 *J. Chem. Phys.* **98** 5648